ELSEVIER

International Journal of Heat and Fluid Flow 22 (2001) 168–179

International Journal of HEAT AND FLUID FLOW

www.elsevier.com/locate/ijhff

Mixed convection in a narrow rectangular cavity with bottom inlet and outlet

Gary Rosengarten, Graham L. Morrison, Masud Behnia *

School of Mechanical and Manufacturing Engineering, The University of New South Wales, Sydney, NSW 2052, Australia

Received 7 December 1999; accepted 14 December 2000

Abstract

A model describing the heat transfer in horizontal mantle heat exchangers used in solar water heaters has been developed by approximating a narrow horizontal annulus to an equivalent rectangular cavity. Particle tracking velocimetry (PTV) and computational fluid dynamics (CFD) simulations were used to determine the flow field. The flow is in the mixed-convection regime, where buoyancy locally affects the flow field and heat flux. The effect of the heat-transfer wall temperature distribution on the net heat-transfer rate has been quantified by the introduction of a stratification correction parameter. A mean Nusselt number, defined by using the difference between the inlet temperature and mean heat-transfer wall temperature, is shown to be independent of buoyancy forces when the stratification correction parameter is taken into account. A correlation has been developed for the mean Nusselt number for a range of geometries and boundary conditions. This correlation predicts the net heat-transfer rate to within 10%. © 2001 Published by Elsevier Science Inc.

Keywords: Cross flow mixed convection; Narrow channel; Heat exchanger; Solar water heater

1. Introduction

The trend in solar domestic water heater design is to incorporate a heat exchanger between the antifreeze collector-loop fluid and the potable water in the storage tank (Dhal and Davidson, 1998; Morrison et al., 1998). The most common designs in Australia, Greece and various other countries use a horizontal mantle heat exchanger (Fig. 1). Horizontal mantle heat exchangers have the hot collector fluid entering a narrow annulus around the storage tank. The flow is generally driven by an induced thermosyphon in the solar collector loop, hence the flow rates are low (<60 l/h). The outer wall of the annulus is insulated, and thus effectively adiabatic, while the inner wall temperature is essentially governed by the temperature of the stored water.

The flow in a mantle heat exchanger can be considered as laminar flow in an annular duct with the inlet and outlet aligned radially so that the inlet flow is directed towards the annulus inner wall. The inlet and outlet pipe diameters are typically 20 times smaller than the mean annulus diameter, and the inlet flow stream, when hotter than the top of the inner wall, rises to the top of the annulus due to buoyancy. The main flow then makes its way through the annulus towards the bottom outlet, transferring heat to the annulus inner wall along the way.

It can be shown that in the limit of the radius ratio, r^*, approaching 1, the forced convective heat transfer in an annular duct approaches that for parallel plates (Shah and London, 1978). The same can be said for flow in a rectangular channel whose aspect ratio approaches infinity (Shah and London, 1978). Because of the low velocities involved, the flow in the mantle heat exchanger is very dependent on the buoyancy forces that arise due to the temperature difference between the inlet fluid and the inner wall. The flow is thus in the classical mixed-convection regime.

The aim of this study is to understand the flow and heat-transfer processes in horizontal mantle heat exchangers. To this end, we have made use of the fact that the mantle heat exchanger has a radius ratio greater than 0.9, so as to approximate the flow in the narrow annulus to that in a rectangular cavity. This approximation is valid even if buoyancy is involved (see Appendix A). Assuming a vertical plane of symmetry, half of the annulus is effectively unwrapped to form a rectangular cavity whose height is equal to half the mean circumference of the annulus. The advantage of this approach is that it is easier to visualise the flow experimentally, and a rectangular geometry is simpler to model numerically.

2. Previous studies

Fundamental solutions to laminar forced convective heat transfer in ducts are well established (Shah and London, 1978). The thermal boundary condition that consists of having one

* Corresponding author. Tel.: +61-2-9385-4253; fax: +61-2-9663-1222.

E-mail addresses: garyr@student.unsw.edu.au (G. Rosengarten), m.behnia@unsw.edu.au (M. Behnia).

0142-727X/01/$ - see front matter © 2001 Published by Elsevier Science Inc.
PII: S0142-727X(00)00087-4

Notation

A	cross-sectional area of cavity $= wH$ (m^2)
c_p	specific heat of fluid (J/kg K)
g	acceleration due to gravity (m/s^2)
Gr_w	Grashof number $= (g\beta(T_{in} - T_{mean})w^3)/v^2$
$\bar{h}$	mean convective heat-transfer coefficient (W/m^2 K)
H	cavity height (m)
L	cavity length (m)
$\dot{m}$	mass flow rate (kg/s)
Nu_w^*	Nusselt number (non-dimensional heat flux) based on cavity width (see Eq. (1))
p	pressure (Pa)
Pr	Prandtl number $= c_p\mu/\kappa$
q	heat-transfer rate (W)
q''	heat flux (W/m^2)
r^*	radius ratio of annulus $= r_{in}/r_{out}$
r_{in}	radius of inner wall of annulus (m)
r_{out}	radius of outer wall of annulus (m)
R	mean radius $= r_{in} + w/2$ (m)
Re_w	Reynolds number based on cavity width $= \dot{m}w/A\mu$
St	stratification correction parameter $= Nu_w^*/Nu_{w,i}^*$ (see Eq. (6))
t	radial coordinate used in annular coordinate system (m)
T^*	non-dimensional temperature $= (T - T_{wall})/(T_{in} - T_{wall})$
T_{in}	cavity inlet temperature (K)
T_{wall}	heat-transfer wall temperature (K)
T_{mean}	mean heat-transfer wall temperature (K)
T_{bot}	temperature at bottom of heat-transfer wall (K)
u	non-dimensional component of velocity in x-direction
v	non-dimensional component of velocity in y-direction
w	non-dimensional component of velocity in z-direction
w	cavity width or annular gap $(r_{out} - r_{in})$ (m)
x	coordinate in direction of w (m)
y	coordinate in direction of H (m)
z	coordinate in direction of L (m)

Greeks

β	volumetric thermal expansion coefficient
ε	heat exchanger effectiveness $= q/q_{max}$
κ	thermal conductivity (W/m K)
η	stratification efficiency ratio (Eq. (3))
η_{st}	stratification efficiency (Eq. (4))
μ	dynamic viscosity (Pa s)
v	kinematic viscosity (m^2/s)
θ	angular coordinate used in annular coordinate system (rad)
Θ	non-dimensional stratification temperature (Eq. (5))

Subscripts

i	isothermal
bot	bottom

Superscripts

$'$	a dash represents non-dimensional coordinates

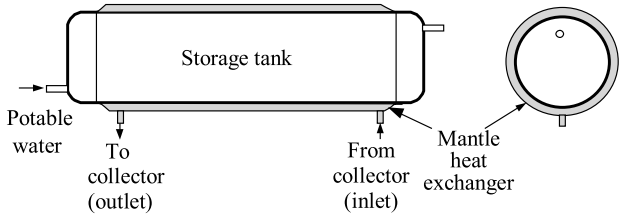

Fig. 1. Schematic of a mantle heat exchanger on a horizontal cylindrical water storage tank.

wall at a constant temperature and the others adiabatic is commonly called a boundary condition of the third kind. The fully developed Nusselt number based on the hydraulic diameter and the log-mean temperature difference is known to be a constant, and is equal to 4.86 for a parallel plate duct with boundary conditions of the third kind. The same value applies to an annular duct with a radius ratio of unity, and similar boundary conditions.

Converting the annular geometry into its rectangular equivalent leaves the heat-transfer surface vertical, so that the natural convection flow is perpendicular to the main bulk flow direction. This combination is called orthogonal (or sometimes cross-flow) mixed convection and has been studied for uniformly heated vertical walls in a rectangular cross-section channel with various restricted inlets and outlets (Neiswanger et al., 1987; Rahman and Carey, 1990; Gao and Rahman, 1999). In these studies, the vertical heat-transfer walls were sufficiently separated to allow the development of a distinct natural convection boundary layer up the vertical wall that was almost de-coupled from the main flow. Accordingly, a heat-transfer correlation was possible in terms of a combination of the Rayleigh and Reynolds numbers. The narrow dimensions of the mantle heat exchanger in this study are such that the forced and free convection boundary layers are not distinct.

Ligrani and Choi (1996) performed an experimental study of mixed convection in straight and curved channels with the buoyancy orthogonal to the main forced flow. They used a high aspect-ratio channel ($H/w = 40$) with uniform heat flux on both sidewalls. They showed that for all cases studied, both in the developing region and for fully developed flow, increasing the Grashof number decreased the Nusselt number. This phenomenon was explained by the decrease in the near wall temperature gradients and the local reduction of streamwise advection velocities near the wall, caused by the buoyancy-induced velocities. This is similar to aligned mixed convection when the buoyancy opposes the flow. They also defined flow regimes that depended on the ratios Gr/Re^2 and $Gr/Re^{0.5}$.

Laminar fully developed mixed convection in an annulus has been studied where one wall had a constant heat flux and the other was insulated (Hattori, 1979). The net heat transfer was found to depend on the Grashof number when it was above a critical value. The maximum radius ratio studied was 0.8. Laminar developing mixed convection in a horizontal annulus has been studied numerically for a radius ratio of 0.5 (Karki and Patankar, 1989). More recently, annuli with radius ratios of 0.25, 0.5 and 0.75 were modelled for water and air using boundary conditions of the second and third kinds (Nonio and Giudice, 1996). These results showed that the effect of the Rayleigh number on the mean Nusselt number decreased with increasing radius ratio, although in the study by Nonio and Giudice (1996) the radius ratio was limited to 0.75.

It is clear that the flow in the mantle heat exchanger is sufficiently different to these idealised cases to warrant a study of its own. Morrison et al. (1998) studied the flow field

numerically and included a limited amount of experimental data. The effect of different parameters such as the inlet position on the flow was established. The flow in a 10 mm wide rectangular cavity has been investigated by Rosengarten et al. (1999a), who showed the behaviour of the flow and the local heat transfer for a limited range of conditions. They concluded that localised turbulence near the inlet has little effect on the local heat transfer below a critical Reynolds number. In the present study, attention is focused on obtaining mean Nusselt number correlations for various-sized rectangular cavities with a range of boundary conditions, that can be easily implemented in solar process simulation software such as TRNSYS (Klein, 1996).

3. Experimental setup

The rectangular cavity ($L \times H = 0.48 \times 0.23$ m^2) used in the experiments consisted of 10 mm thick Plexiglas front and side walls, and a 10 mm thick copper heat-transfer wall (Fig. 2). The gap widths (w) used were 5 and 10 mm, with inlet and outlet diameters of 10 or 15 mm. The temperature of the heat-transfer wall was maintained by temperature-controlled water flowing through two independent channels connected to the back of the heat exchanger surface. Twenty-seven calibrated type T thermocouples were embedded in the heat-transfer wall, with their tips approximately 2 mm from the front surface. The thermocouples were positioned in three columns of 9, spanning the height of the cavity. The thermocouple columns were aligned with the inlet at $z = 25$ mm, the centre at $z = 240$ mm and the outlet at $z = 455$ mm (see Fig. 2). A thermocouple was installed at the centre of both the inlet and outlet pipes, about 20 mm from the front wall of the cavity. A closed-loop temperature-controlled water tank was used to control the water circulation through the cavity. The flow was controlled with an actuator valve and measured with a calibrated turbine flow meter. The effect of the Prandtl number was investigated by replacing the water in the tank with a 20% propylene glycol/water mixture, which is common in solar water heater collectors/heat exchanger loops.

The velocity field in the cavity was measured using particle tracking velocimetry (PTV) with a 1 mm thick light sheet, produced by a 22 mW HeNe laser and a cylindrical lens. The front of the cavity was divided into four quarters for PTV measurements. This viewing size allowed reasonable resolution of the seed particles and adequate illumination from the light sheet. Plastic seed particles with diameters in the range of 100–200 μm, and specific gravity of 0.99 at 20°C, were used. Images were recorded with a digital video camera and downloaded to a PC using a Scion LG3 capture card and Scion Image software. The image software's particle centre finding utility was used to find the particle centres and a program was written to trace particles and calculate velocities.

Streak lines were also obtained by averaging approximately 50 video frames of particle positions over a period of around 12 s. As the flow structure in the outlet half of the cavity did not vary noticeably with the different boundary conditions used, for the present study PTV was performed on the inlet half of the cavity only.

4. Analysis

4.1. Numerical model

The commercial CFD package FLUENT V4.4 (Fluent Inc., 1997) was used to simulate the flow and heat transfer. The continuity and momentum equations along with the transport equation for static enthalpy were solved using finite volumes. The Boussinesq approximation for buoyancy was used in all the cases. Although it has been shown that turbulence has a minor effect on the local heat transfer near the inlet for the higher range of inlet flow rates in mantle heat exchangers (Rosengarten et al., 1999a), this study deals with the net heat transfer where the effect of turbulence is negligible. Furthermore, changing from a 10 to a 5 mm wide cavity decreased the turbulent intensity by a factor of 10, so that turbulence did not affect the heat transfer at all. Thus, only laminar flow was modelled.

A $79 \times 41 \times 19$ grid ($L \times H \times$ w), making up 62,000 grid points, was used in the computations. The grid distribution was finer near the inlet and outlet where the velocity and temperature gradients were higher. A grid-sensitivity test revealed that doubling the number of grid points in any

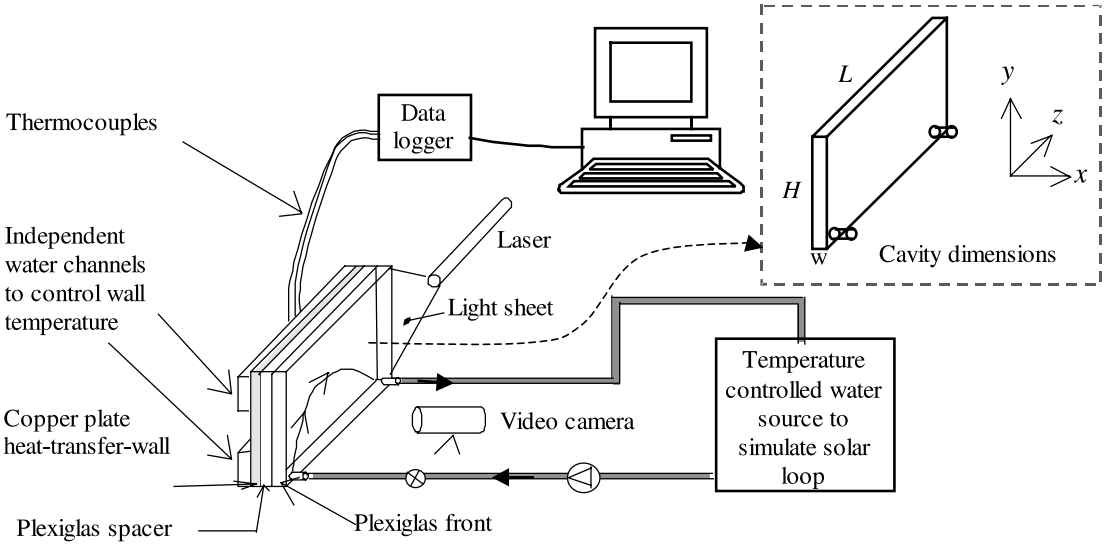

Fig. 2. Experimental set-up for heat transfer and PTV measurements in a rectangular cavity. The flow rate was varied from 0.002 to 0.015 kg/s, the wall temperature from 20–50°C and the inlet temperature from 20–50°C.

two dimensions changed the net heat transfer rate by less than 2%.

4.2. Definition of Nusselt number

Duct flow mean Nusselt numbers for boundary conditions of the third kind are generally calculated using the log-mean temperature difference between the inlet and outlet and the wall. However, as pointed out by Mercer et al. (1967), this definition is not always the most useful for design purposes, as it requires knowledge of both the inlet and outlet temperatures. A Nusselt number based on the temperature difference between the inlet fluid and the wall temperature requires less information and is therefore generally more useful for designers. In some literature the Nusselt number based on this definition is referred to as the non-dimensional heat flux (Shah and London, 1978). It is this number which is used in our analysis in order to allow simple evaluation of the net heat transfer, given the flow rate and the inlet and heat-transfer wall temperatures, and it is distinguished from a classical Nusselt number by the superscript *. It is given by

$$Nu_w^* = \frac{q''_{mean} w}{\kappa(T_{in} - T_{mean})}. \quad (1)$$

Using this definition means that the Nusselt number is not a constant for fully developed duct flow. It can be shown (Morrison et al., 1999) that for forced fully developed flow in a rectangular duct with boundary conditions of the third kind, the Nusselt number given by Eq. (1) is

$$Nu_w^* = \frac{w\dot{m}c_p}{\kappa HL}\left(1 - \exp\left(-\frac{HL\bar{h}}{\dot{m}c_p}\right)\right) = Re_w Pr \frac{w}{L}\left(1 - \exp\left(\frac{-1}{Re_w Pr}\frac{L\bar{h}}{\kappa}\right)\right). \quad (2)$$

Note that when Eqs. (1) and (2) were used with our data, the inlet temperature was based on the temperature at the inlet to the cavity. This is different from using a bulk mean temperature at the entrance to a duct, which is what was assumed in the derivation of Eq. (2), so that $\bar{h}$ is not a standard convective heat-transfer coefficient.

4.3. Quantifying stratification

For this study we set out to examine the effect of different vertical temperature distributions, or different degrees of stratification of the heat-transfer wall, on the net heat-transfer rate in the cavity. Kays and Crawford (1980) outlined an analytical solution for hydrodynamically fully developed forced laminar convection in ducts with arbitrary axial temperature distributions. They also showed the effect of arbitrary plate temperature distributions for forced and free convective boundary layer flows on flat plates, however only cases with the simplest temperature distributions could be solved analytically. As we are dealing with cross-flow, where the wall temperature variation is not in the direction of the main flow, and where the temperature distribution can be a complicated function of height, the problem is more complex.

In mantle heat exchangers the heat-transfer wall temperature distribution is controlled by the temperature in the tank, which, due to thermal stratification, is always cooler at the bottom than at the top. Using a second law analysis, Rosengarten et al. (1999b) defined a parameter called the stratification efficiency to describe the degree of stratification in storage tanks. The stratification efficiency has been adapted for this study to form the stratification efficiency ratio which is given by

$$\eta = \frac{\eta_{st}}{\eta_{st,i}}, \quad (3)$$

where

$$\eta_{st} = 1 - \frac{T_{in}}{H(T_{in} - T_{mean})}\int_0^H \ln\left(\frac{T_{in}}{T_{wall}(y)}\right) dy \quad (4)$$

and $\eta_{st,i}$ is the value of η_{st} for an isothermal heat-transfer wall with the same mean temperature as a non-isothermal heat-transfer wall. Thus, for an isothermal heat-transfer wall $\eta = 1$.

Other parameters that have been used to describe linear stratification have generally been in the form of

$$\Theta = \frac{T_{in} - T_{bot}}{T_{in} - T_{mean}} \quad (5)$$

(see for example Bejan, 1995 or Zenen et al., 1985).

We will show that while Eq. (5) can be used to scale the degree of linear stratification, it cannot scale the degree of stratification in many real systems where the temperature distribution is often far from linear.

4.4. Nusselt number scaling

Due to the three-dimensional nature of the cavity flow, it is not obvious what the characteristic scaling dimension should be. The flow enters the cavity perpendicular to the mean flow plane, as a low velocity impinging jet with buoyancy. The inlet stream then rises up the cavity and starts to move horizontally towards the outlet. In order to be consistent with other duct flow data the cavity width, w, has been used as the characteristic length.

5. Results and discussion

Initially we were interested in obtaining the dependence of the net heat transfer rate on the flow rate while keeping all other variables constant. Fig. 3 is a plot of Nu_w^* calculated from

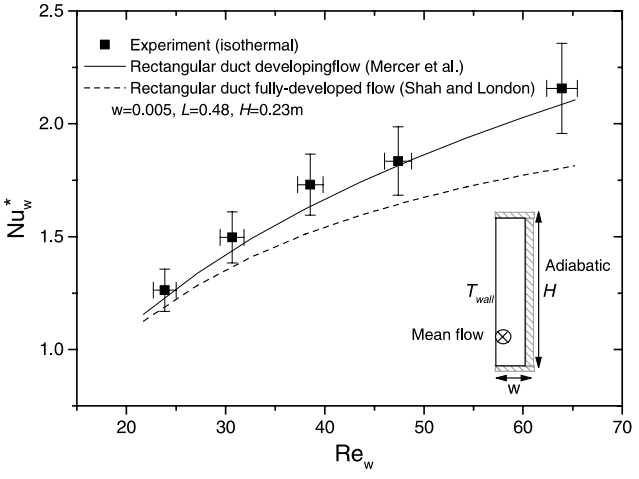

Fig. 3. Experimentally obtained mean Nusselt number as a function of Reynolds number for a rectangular cavity with an isothermal wall (see Fig. 2). Error bars represent uncertainties in the measured data, calculated at a 95% level of confidence. Also plotted are the values of the mean Nusselt number for fully developed flow and hydrodynamically and thermally developing flow in a rectangular duct of the same dimensions.

our experimental data for the rectangular cavity with an isothermal heat-transfer wall, along with the theoretical Nusselt number calculated using Eq. (2). The only unknown in Eq. (2) is the convective heat-transfer coefficient, $\bar{h}$. The fully developed value was obtained from Shah and London (1978) (see Fig. 39 of their book), and used for the dashed curve in Fig. 3. The solid curve utilizes the values of $\bar{h}$ for developing flow given by Mercer et al. (1967). As shown in Fig. 3 the variation of Nu_w^* with Reynolds number for the rectangular cavity is close to that predicted by simple one-dimensional duct flow theory. This may seem somewhat surprising considering that the nature of the flow in the inlet region is far from one-dimensional. However for most of the heat exchanger surface, the flow is parallel to the heated heat-transfer wall and is driven purely by the pressure difference. The nature of the flow and heat transfer will be discussed in more detail in later sections.

5.1. Validation of numerical results

The measured flow field in the mid-plane of the cavity for both isothermal and stratified heat-transfer wall conditions is shown in Figs. 4 and 5. The experimental results show streak lines obtained by averaging 50 video frames (Figs. 4(b) and 5(b)), spaced at 0.2 s intervals. Also shown are the PTV velocity vectors (Figs. 4(a) and 5(a)), which show reasonable agreement, both in direction and magnitude, with the numerically obtained velocity vectors (Figs. 4(c) and 5(c)). One noticeable difference between the experimental results and the numerical results is the small eddy that is shown in Fig. 4(c) in the top left-hand corner but not picked up by the PTV. This is because, as shown in Fig. 4(b), there are very few particles needed for PTV measurements in that corner, meaning that the particle-laden inlet flow did not penetrate into that region.

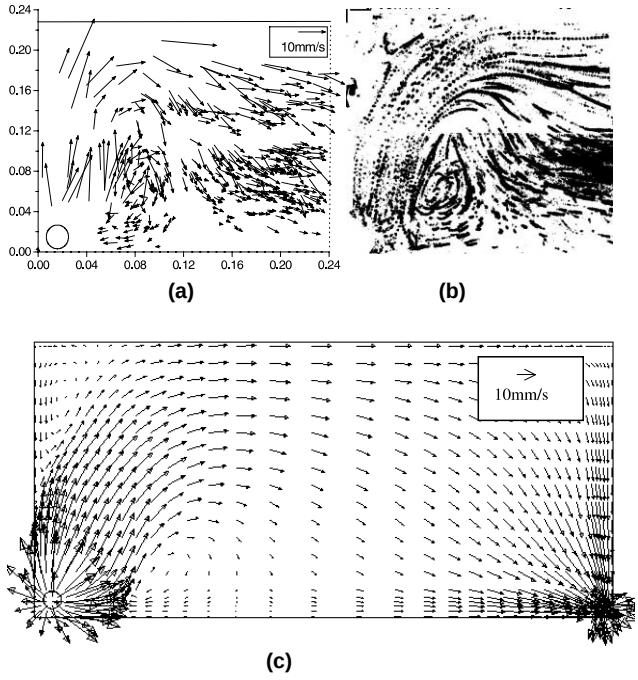

Fig. 4. Comparison of experimentally determined velocity vectors and streak lines with numerically calculated velocity vectors for an isothermal wall at 25°C, cavity inlet temperature of 35°C, and flow rate of 7.0×10^{-3} kg/s. (a) PTV velocity vectors in inlet half of cavity. (b) Streak lines obtained by averaging 50 video frames. (c) Velocity vectors obtained numerically.

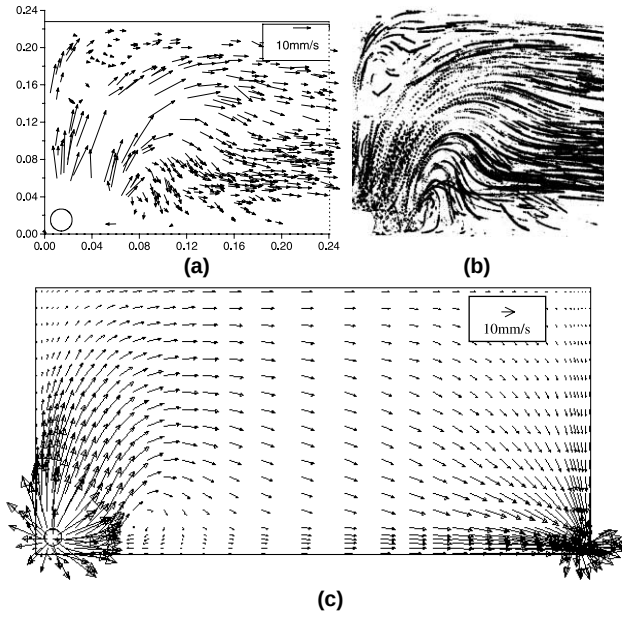

Fig. 5. Comparison of experimentally determined velocity vectors and streak lines with numerically calculated velocity vectors for a stratified wall from 20–30°C, cavity inlet temperature of 30°C and flow rate of 6.5×10^{-3} kg/s. (a) PTV velocity vectors in inlet half of cavity. (b) Streak lines obtained by averaging 50 video frames. (c) Velocity vectors obtained numerically.

With very few particles in that corner, it was difficult to capture the low-velocity recirculation zone. Other discrepancies are indicative of the fact that there are considerable uncertainties associated with aligning a 1 mm thick laser sheet into the centre of a 5 mm wide cavity. Slight misalignment can result in considerable errors due to the large velocity gradients in the x-direction.

Comparison of the net heat-transfer rate between the numerical and experimental results is shown in Fig. 6. The nu-

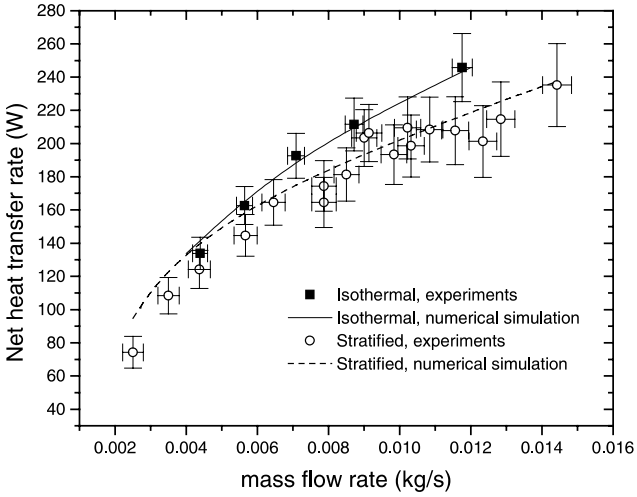

Fig. 6. Comparison of the net heat-transfer rate as a function of mass flow-rate. The isothermal results are for a 35°C cavity inlet and 25°C wall. The stratified results are for 20–30°C wall stratification and 30°C cavity inlet. Error bars represent uncertainties in the measured data, calculated at a 95% level of confidence (from temperature measurement uncertainty and flow-rate measurement uncertainty).

merical results are in good agreement with the experimental results over a wide range of flow rates. The numerical results tend to slightly overestimate the heat transfer rate at lower flow rates, probably because in the numerical simulations the outer walls were set as adiabatic. In the experiments, the outer walls are not perfectly insulated and the ratio of the heat loss to the surroundings relative to the net heat-transfer rate is exacerbated at lower flow rates.

5.2. Flow field and heat flux

As Figs. 4 and 5 show, there is little difference in the flow field between the isothermal and stratified cases, except that more flow enters the top regions in the isothermal case. This is because the buoyancy force (proportional to temperature difference between cavity fluid and heat-transfer wall) remains almost constant up to the top of the cavity for the isothermal cases, while it decreases for the stratified case due to the decreasing difference in temperature between the inlet flow and the heat-transfer wall.

Although the flow is similar in the isothermal and stratified cases, the isotherms and the heat flux contours are significantly different (Fig. 7). For the isothermal case, the hot incoming fluid rises to the top and thus most of the heat transfer is in the top region of the cavity (Fig. 7(b)). The near-horizontal isotherms for the stratified conditions in Fig. 7(c) show that the inlet flow barely disturbs the stable stratification set up by the heat-transfer wall temperature distribution. Once the hot inlet stream reaches the top of the cavity, the temperature of the fluid is close to the heat-transfer wall temperature, and thus there is negligible heat transfer in the top region of the cavity (Fig. 7(d)).

The effect of flow rate for the isothermal case is shown in Fig. 8 (the stratified case is not shown here, as the effect is similar). The main feature of the flow is the mixed convective plume above the inlet which, as the flow rate is increased, changes from being a buoyancy-dominated near-vertical plume (Fig. 8(a)) into being almost evenly spread over the heat-transfer wall (Fig. 8(d)). For the lower flow rates (Figs. 4(c), 5(c) and 8(a)), most of the flow above the inlet is confined to a small stream with velocities much greater than the average velocity in the rest of the cavity (bulk flow), so that a recirculation zone is developed by entrainment of the bulk flow into the inlet stream.

The high heat flux region around the inlet with an area of about 7% of the total heat-transfer area, represents 12% and 18% of the total heat transfer for the isothermal and stratified cases, respectively (with boundary conditions as in Figs. 4 and 5). This shows that the impinging inlet flow has an effect on, but does not dominate, the net heat transfer in the cavity.

5.3. Effect of stratification

The effect of stratification – or a non-isothermal heat-transfer wall temperature distribution – on the net heat-transfer rate is significant. When the difference between the inlet temperature and mean heat-transfer wall temperature is the same, stratification tends to increase the heat-transfer rate. This effect is shown in Fig. 9(a), where the net heat-transfer rate relative to that of an isothermal heat-transfer wall, called the stratification correction parameter St, is plotted as a function of the non-dimensional stratification temperature, Θ, for various degrees of stratification (all with the same mean temperature and the same Reynolds number). As illustrated in Fig. 9(a), Θ does not account for different wall temperature distributions that have the same top and bottom temperatures. Hence, to correctly determine the degree of stratification, the stratification efficiency ratio defined in Eq. (3) should be used instead of Θ.

The effect of stratification also depends on the Reynolds number, as shown in Fig. 9(b). Increasing the Reynolds number decreases the effect of stratification. Consequently, natural convection must play a role in the effect of stratification on the heat-transfer rate, in that increasing the Reynolds number decreases the proportion of the natural convection component of the heat transfer. A power law was fitted to the

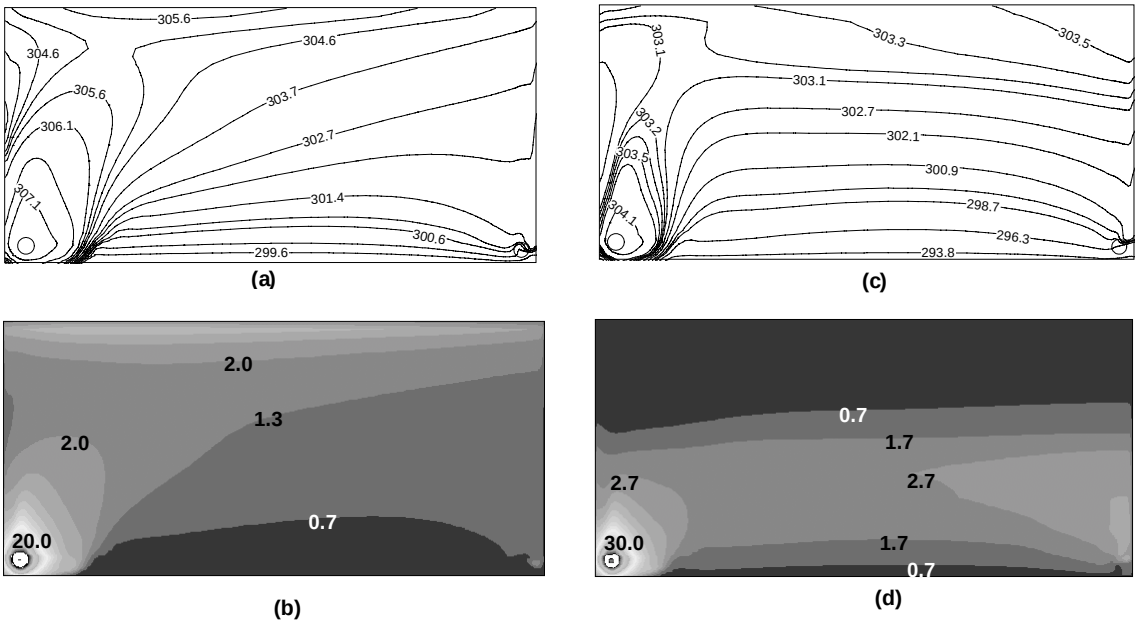

Fig. 7. Numerical simulation of temperature contours in the mid-plane of the cavity and heat flux into the wall. (a) Temperature contours (K) for the same conditions (isothermal) as Figs. 5(a)–(c). (b) Corresponding heat flux contours (kW/m^2). (c) Temperature contours (K) for the same conditions (stratified) as Figs. 6(a)–(c). (d) Corresponding heat flux contours (kW/m^2).

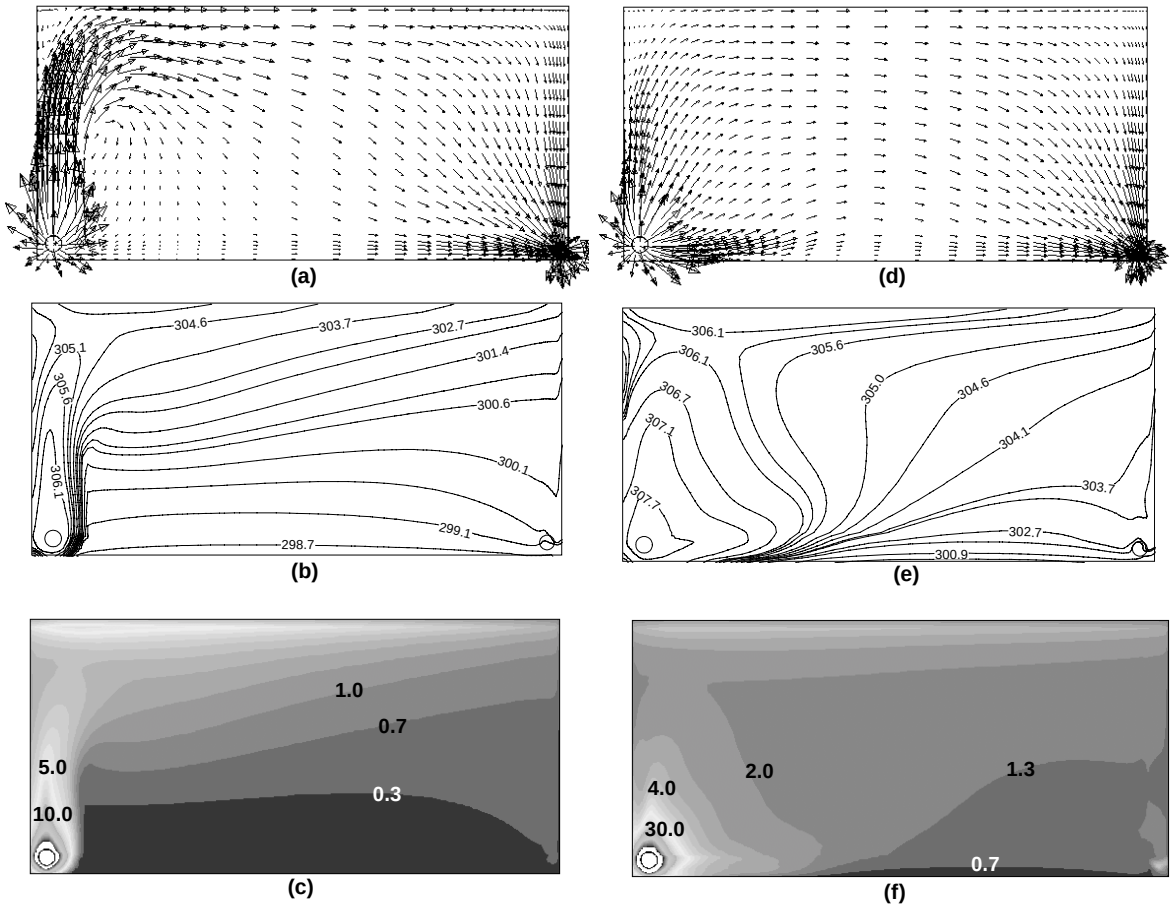

Fig. 8. Numerical simulation of 25°C isothermal wall and 35°C cavity inlet flow. (a) Velocity vectors in the mid-plane for an inlet flow rate of 4.0×10^{-3} kg/s. (b) Temperature contours (K) in the mid-plane of the cavity with the same conditions as Fig. 8(a). (c) Corresponding heat flux contours (kW/m^2). (d) Velocity vectors in the mid-plane for a flow rate of 1.2×10^{-2} kg/s. (e) Temperature contours in the mid-plane of the cavity with the same conditions as Fig. 8(d). (f) Corresponding heat flux contours (kW/m^2).

dependence of St on the Reynolds number and the exponent was found to be a function of the stratification efficiency ratio, η. An overall equation was developed to take into account the Reynolds number effect along with the stratification effect, and the collapsed data are shown in Fig. 10. The full stratification correction parameter is given in Eq. (6), where logarithmic functions are used to reflect the logarithmic nature of the stratification efficiency (Eq. (4)).

$$\mathrm{St} = \frac{Nu^*_{\mathrm{w}}}{Nu^*_{\mathrm{w,i}}} = Re^{-0.176(\ln \eta)^{0.3}}(1 + 2.268(\ln \eta)^{0.56}). \quad (6)$$

5.4. Effect of buoyancy on heat transfer

As the previous results have shown, buoyancy has a significant effect on the flow field and local heat-transfer rate. To test the effect of buoyancy on the net heat-transfer rate, the ratio $Gr_{\mathrm{w}}/Re^2_{\mathrm{w}}$, which is generally regarded as a parameter that measures the relative magnitude of the free and forced components of convection (see Eq. (A.3)), was varied from 0.1 to 5000 in the numerical simulations. This range represents limiting values found in mantle heat exchangers used in solar water heaters. It would appear from Eqs. (A.6)–(A.9) that the rectangular analogy to the annular geometry is not valid when $Gr_{\mathrm{w}}/Re^2_{\mathrm{w}}$ is large. However, as shown in Fig. 15 the heat flux distribution with height varies little between the rectangular and annular cases (see further discussion of this point in Appendix A). It is important to note here that the Grashof numbers are higher than those based on a local mean temperature in the cavity because they are based on an inlet temperature, not on a mean fluid temperature in the cavity. A local Grashof number would be smaller, as the mean fluid temperature in the cavity is considerably lower than the inlet temperature (see Figs. 7(a) and (c) for example). Fig. 11 shows that natural convection in the cavity has a negligible effect on the mean Nusselt number (in the range $1 < Re_{\mathrm{w}} < 100$), when the $Gr_{\mathrm{w}}/Re^2_{\mathrm{w}}$ ratio is varied by three orders of magnitude, and the stratification correction parameter has been used. It is possible to conclude that the data are independent of $Gr_{\mathrm{w}}/Re^2_{\mathrm{w}}$, and thus independent of buoyancy effects, as long as the data form a single smoothly connected curve. Thus, the variation of the data from a linear curve is not significant in this instance.

While the mean stratification-corrected Nusselt number for these cases is independent of buoyancy, the local conditions are affected by natural convection (see, for example, Fig. 8). The effect of buoyancy can be seen in Fig. 12, where the local heat flux obtained from numerical simulations has been averaged along the length of the cavity, and plotted as a function of height, with and without buoyancy forces included. Buoyancy tends to distribute the heat to higher levels of the heat-transfer wall; however when the stratification correction parameter is

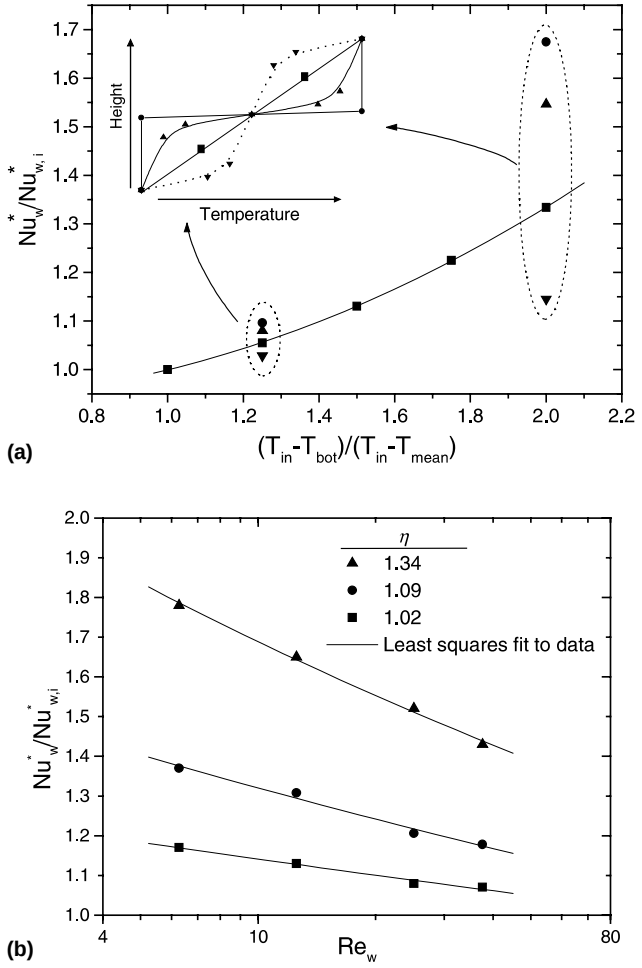

Fig. 9. The dependence of the ratio of net Nusselt number in a cavity with a stratified wall to that with an isothermal wall with the same mean temperature ($Nu_w^*/Nu_{w,i}^*$) called the stratification correction parameter, St. (a) Variation of St with the degree of stratification in the heat-transfer wall, measured with the non-dimensional stratification temperature, Θ, for a Reynolds number of 36. (b) Variation of St with Re for various values of η.

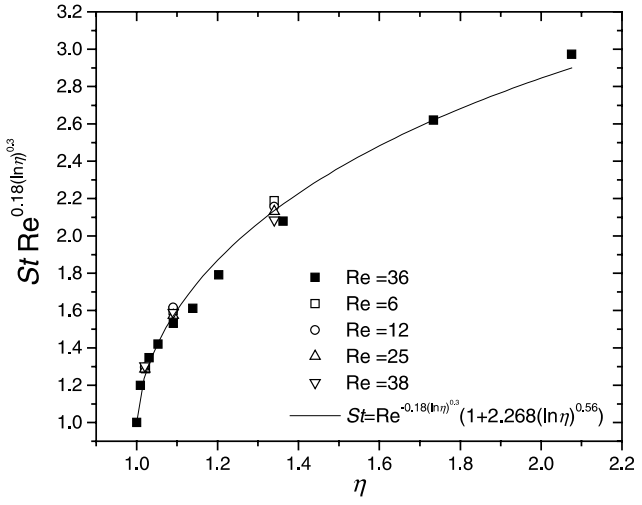

Fig. 10. Variation of St with η including a correction for the effect of Reynolds number calculated from Fig. 9(b).

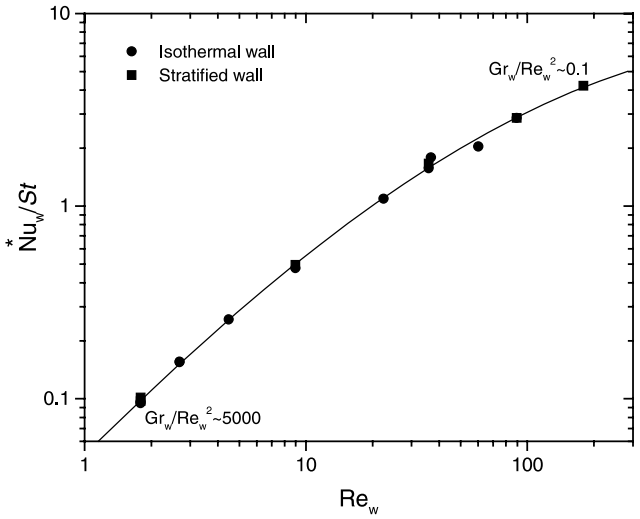

Fig. 11. Nusselt number versus Reynolds number for a range of Gr_w/Re_w^2, for both an isothermal wall and a stratified wall. The line represents a third-order least-squares line of best fit to the data.

taken into account, the net heat-transfer rate, obtained from integration of the curves in Fig. 12, is approximately the same with and without buoyancy forces. The reason why the mean Nusselt number is independent of buoyancy will be discussed in Section 5.7.

5.5. Effect of geometry

All the dimensions of the cavity were varied to ascertain the effect on the net heat-transfer rate. Three inlet-port diameters were tested – 10, 15 and 25 mm – with no noticeable change in the net heat transfer rate. The independence of the net heat-transfer rate on the inlet port diameter confirms that the impinging jet has only a small effect on the net heat-transfer rate for the range of inlet velocities considered here.

The length, width and height of the cavity were varied in the numerical simulations while the mass flow rate was kept constant, to determine how the Nusselt number varies with cavity dimensions. Eq. (2) was fitted to the simulation results for the Nusselt number, with the only unknown being the mean convective heat-transfer coefficient, $\bar{h}$. With $\bar{h} = 363$ W/m^2 K, Eq. (2) fit the data well, as shown in Fig. 13.

5.6. Nusselt number correlation

Combining the results and including the stratification correction leads to an overall Nusselt number correlation for a wide variety of conditions as shown in Fig. 14. The Nusselt number is a function of the Reynolds number, Prandtl number, the cavity dimensions and the heat-transfer wall temperature distribution, and is given by

$$Nu_w^* = Re_w Pr\,\mathrm{St}\frac{w}{L}\left(1-\exp\left(\frac{-1}{Re_w Pr}\frac{363L}{\kappa}\right)\right) \tag{7}$$

with St defined in Eq. (6).

The Nusselt number obtained using this equation agrees with the experimental and numerical simulation data to within 10% for $5 \leqslant Pr \leqslant 14$, $1 \leqslant Re_w \leqslant 100$, $w/L < 0.02$ and $w/H < 0.07$. All fluid properties are calculated at the average of the inlet temperature and the mean heat-transfer wall temperatures.

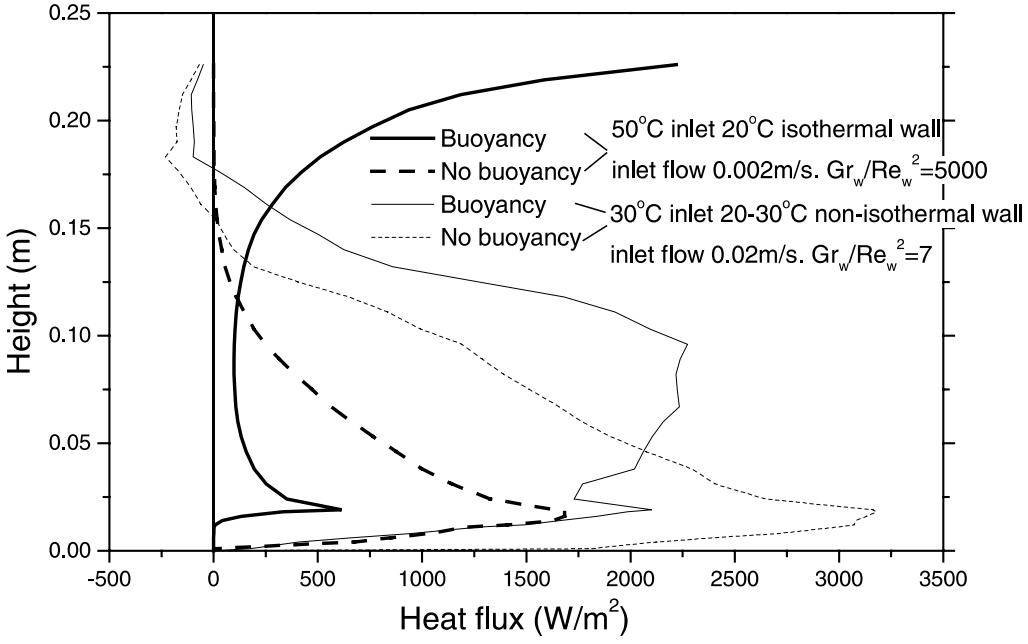

Fig. 12. Axially (in the z-direction) averaged heat flux, calculated from numerical simulations, as a function of height for two different boundary conditions, with and without buoyancy.

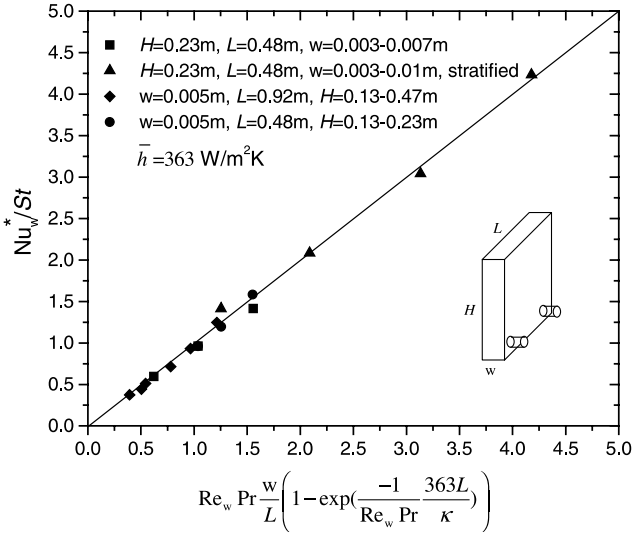

Fig. 13. Calculated Nusselt number (from numerical simulations) versus theoretical Nusselt number for a variety of cavity sizes.

5.7. Heat exchanger effectiveness

The maximum possible heat-transfer rate used in the calculation of the heat exchanger effectiveness, ε, occurs when the outlet temperature equals the wall temperature for an isothermal heat-transfer wall, or the temperature at the bottom of the wall for a non-isothermal (stratified) heat-transfer wall. This being the case, the heat exchanger effectiveness can easily be calculated using Eq. (7).

In a 0.23 m by 0.48 m cavity with an isothermal heat-transfer wall, when the flow rate is low (which is when natural convection effects would be expected to be large), the effectiveness is in the order of 0.95. This means that the net heat-transfer rate is almost at its maximum due to forced convection only. Therefore, at best, natural convection can only add an extra 5% to the net heat-transfer rate. As the flow rate is increased the effectiveness decreases, but any increase to the heat transfer rate due to natural convection is much smaller than the increased heat-transfer rate associated with the higher flow rates. The effectiveness for the stratified case is considerably lower for the same flow rate (approximately 20–30% lower for the conditions in the experiments – see Figs. 5–8). Therefore natural convection can potentially increase the heat-transfer rate when the heat-transfer wall is stratified. This explains why the stratification correction parameter, given in Eq. (5), has a Reynolds number dependence that increases as the Reynolds number is decreased. The Reynolds number dependence effectively takes into account the additional heat-transfer rate provided by natural convection for cases when the heat-transfer wall is not isothermal. Thus Nu^*_w/St, as shown in Fig. 11, is independent of buoyancy.

6. Conclusions

1. For very narrow annuli ($r^* > 0.9$), the flow and heat transfer can be well approximated by using a rectangular cavity with the same gap width as the annulus, and whose height is equal to half of the mean annular circumference.
2. The conditions in mantle heat exchangers used in solar water heaters are very different to standard axial duct flow, yet it has been shown that the net heat-transfer characteristics are very similar.
3. The effect of stratification on the heat-transfer rate in a rectangular cavity with a bottom inlet relative to that with an isothermal heat-transfer wall has been quantified. A stratification correction parameter has been suggested for use in correlations.
4. Buoyancy has a significant effect on the flow field and heat flux distribution in the rectangular cavity. However, for the range of parameters and cavity sizes considered here, if the

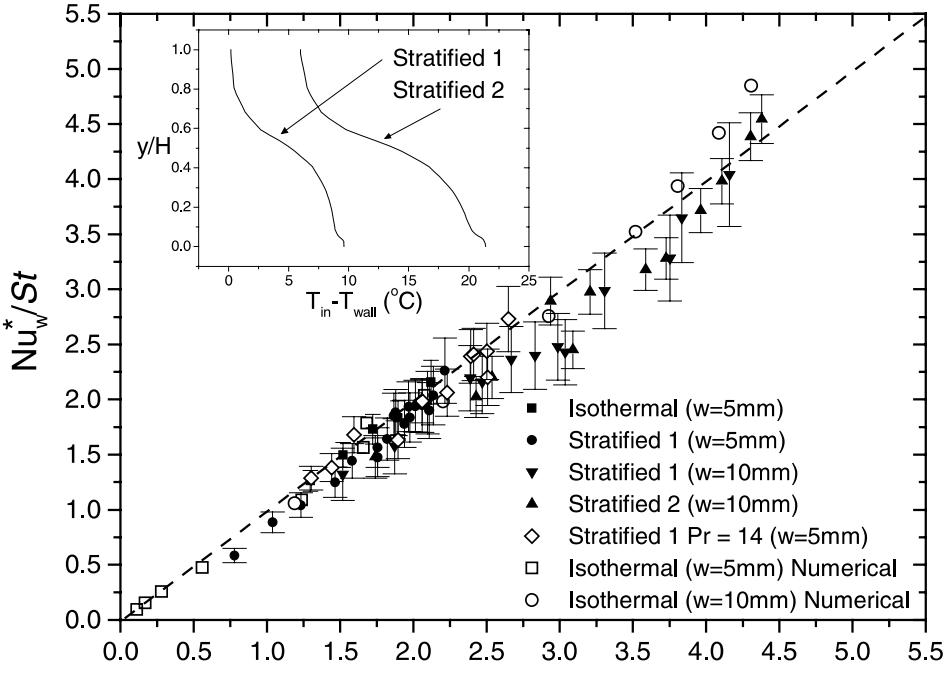

$$\mathrm{Re_w}\,\mathrm{Pr}\frac{\mathrm{w}}{L}\left(1-\exp\left(\frac{-1}{\mathrm{Re_w}\,\mathrm{Pr}}\frac{363L}{\kappa}\right)\right)$$

Fig. 14. Comparison of measured and simulated Nusselt numbers with the predicted value using the overall correlation. The dotted line is the equality line. The two stratified wall temperature distributions are shown on the inset graph. All results are for water with a $Pr \sim 6$, except for the data indicated which is propylene glycol with $Pr \sim 14$.

newly defined stratification correction parameter is taken into account, the mean modified Nusselt number, Nu^*_w is a function of the Reynolds number only. This is shown to be due to the high heat exchanger effectiveness for the range of conditions considered.

5. The mean Nusselt number for rectangular cavities with a wide variety of boundary conditions and geometries, can now be predicted using a correlation in terms of the Reynolds number, Prandtl number, cavity dimensions and heat-transfer wall temperature.

Appendix A. Annular to rectangular transformation

In order to determine the relationship between the flow and heat transfer characteristics in a narrow annular cavity relative to those in a rectangular cavity, an annular coordinate system is introduced. The relationship between the annular coordinate system and Cartesian coordinates is

$$x = (R+t)\cos\theta \quad \text{and} \quad y = (R+t)\sin\theta, \tag{A.1}$$

where z and θ have the same definitions as for a standard cylindrical coordinate system, and instead of the radial coordinate, r, there is a constant mean radius R, and variable radial coordinate value t.

If this coordinate system is used, and the Boussinesq approximated Navier–Stokes equations are non-dimensionalised by letting $u = u_t/V$, $v = u_\theta/V$, $w = u_z/V$, $p' = p/(\rho_\infty V^2)$ (this characteristic pressure implies that the dominant forces will be inertia and buoyancy),

$$x' = q/\mathrm{w}, \quad y' = R\theta/\mathrm{w}, \quad z' = z/\mathrm{w} \quad \text{and}$$
$$T^* = \frac{T - T_{\mathrm{wall}}}{T_{\mathrm{in}} - T_{\mathrm{wall}}} = \frac{\Delta T}{T_{\mathrm{in}} - T_{\mathrm{wall}}},$$

where V is some characteristic velocity, w is the gap width and T_{wall} is the inner wall temperature, the radial component of the momentum equations is

$$u\frac{\partial u}{\partial x'} + \frac{vR}{(\frac{R}{\mathrm{w}}+x')\mathrm{w}}\frac{\partial u}{\partial y'} + w\frac{\partial u}{\partial z'} - \frac{v^2}{(\frac{R}{\mathrm{w}}+x')} = \frac{Gr_{\mathrm{w}}}{Re_{\mathrm{w}}^2}\sin\theta T^* - \frac{\partial p'}{\partial x'} + \frac{1}{Re_{\mathrm{w}}}\left(\nabla^2 u - \frac{u}{(\frac{R}{\mathrm{w}}+x')^2} - \frac{2R}{\mathrm{w}(\frac{R}{\mathrm{w}}+x')^2}\frac{\partial v}{\partial y'}\right). \tag{A.2}$$

Now we are in a position to determine what happens when w/R becomes very small.

Performing a Taylor series expansion on the w/R terms in Eq. (A.2) gives

$$\frac{1}{(\frac{R}{\mathrm{w}}+x')} = \frac{\mathrm{w}}{R}\frac{1}{\left(1+\frac{x'R}{\mathrm{w}}\right)} = \frac{\mathrm{w}}{R}\left(1 - \frac{x'\mathrm{w}}{R} + \mathrm{O}\left(\frac{x'\mathrm{w}}{R}\right)^2 + \cdots\right). \tag{A.3}$$

Because $\mathrm{w}/R \ll 1$ and $|x'| \leqslant 1/2$, we can neglect all terms greater than first order in w/R. Therefore only the first term on the right-hand side of Eq. (A.3), w/R, will be significant. Using this approximation in Eq. (A.2) yields

Table 1
Non-dimensionalised Boussinesq approximated Navier–Stokes and energy equations for a rectangular cavity in rectangular coordinates (left) and a narrow annular cavity in annular coordinates (right)[a]

Rectangular		Annular	
$\frac{\partial u}{\partial x}+\frac{\partial v}{\partial y}+\frac{\partial w}{\partial z}=0$	(A.5)	$\frac{\partial u}{\partial x}+\frac{\mathrm{w}}{R}\frac{\partial u}{\partial x}+\frac{\partial v}{\partial y}+\frac{\partial w}{\partial z}=0$	(A.6)
$u\frac{\partial u}{\partial x}+v\frac{\partial u}{\partial y}+\mathrm{w}\frac{\partial u}{\partial z}=-\frac{\partial p}{\partial x}+\frac{1}{Re_{\mathrm{w}}}(\nabla^2 u)$	(A.7)	$u\frac{\partial u}{\partial x}+v\frac{\partial u}{\partial y}+w\frac{\partial u}{\partial z}-\frac{\mathrm{w}}{R}v^2=\frac{Gr_{\mathrm{w}}}{Re_{\mathrm{w}}^2}\sin\theta T^*-\frac{\partial p}{\partial x}+\frac{1}{Re_{\mathrm{w}}}\left(\nabla^2 u-\frac{2\mathrm{w}}{R}\frac{\partial v}{\partial y}\right)$	(A.8)
$u\frac{\partial v}{\partial x}+v\frac{\partial v}{\partial y}+w\frac{\partial v}{\partial z}=\frac{Gr_{\mathrm{w}}}{Re_{\mathrm{w}}^2}T^*-\frac{\partial p}{\partial y}+\frac{1}{Re_{\mathrm{w}}}(\nabla^2 v)$	(A.9)	$u\frac{\partial v}{\partial x}+v\frac{\partial v}{\partial y}+w\frac{\partial v}{\partial z}-\frac{\mathrm{w}}{R}uv=\frac{Gr_{\mathrm{w}}}{Re_{\mathrm{w}}^2}\cos\theta T^*-\frac{\partial p}{\partial y}+\frac{1}{Re_{\mathrm{w}}}\left(\nabla^2 v-\frac{2\mathrm{w}}{R}\frac{\partial v}{\partial y}\right)$	(A.10)
$u\frac{\partial w}{\partial x}+v\frac{\partial w}{\partial y}+w\frac{\partial w}{\partial z}=-\frac{\partial p}{\partial z}+\frac{1}{Re_{\mathrm{w}}}(\nabla^2 w)$	(A.11)	$u\frac{\partial w}{\partial x}+v\frac{\partial w}{\partial y}+w\frac{\partial w}{\partial z}=-\frac{\partial p}{\partial z}+\frac{1}{Re_{\mathrm{w}}}(\nabla^2 w)$	(A.12)
$u\frac{\partial T}{\partial x}+v\frac{\partial T}{\partial y}+w\frac{\partial T}{\partial z}=\frac{1}{PrRe_{\mathrm{w}}}\nabla^2 T$	(A.13)	$u\frac{\partial T}{\partial x}+\left(\frac{\mathrm{w}}{R}\right)v\frac{\partial T}{\partial y}+w\frac{\partial T}{\partial z}=\frac{1}{PrRe_{\mathrm{w}}}\nabla^2 T$	(A.14)
$\nabla^2=\frac{\partial^2}{\partial x^2}+\frac{\partial^2}{\partial y^2}+\frac{\partial^2}{\partial z^2}$		$\nabla^2=\frac{\partial^2}{\partial x^2}+\frac{\mathrm{w}}{R}\frac{\partial}{\partial x}+\frac{\partial^2}{\partial y^2}+\frac{\partial^2}{\partial z^2}$	

[a] Symbols for the non-dimensional variables were chosen to be the same for both the rectangular and annular co-ordinate systems.

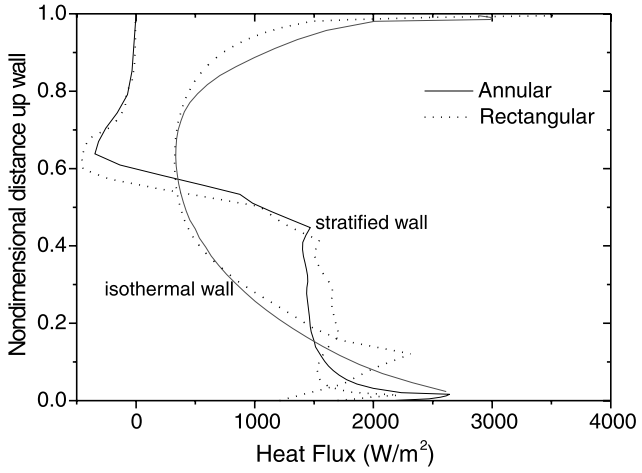

Fig. 15. Average heat flux as a function of height for an annular mantle compared to the equivalent rectangular cavity. $w=0.005$, $H=0.46$, $L=0.92$ m. $Gr_{\mathrm{w}}/Re_{\mathrm{w}}^2$ is 700 for the isothermal case and 50 for the stratified case.

$$u\frac{\partial u}{\partial x'}+\left(\frac{\mathrm{w}}{R}\right)\frac{R}{\mathrm{w}}v\frac{\partial u}{\partial y'}+\mathrm{w}\frac{\partial u}{\partial z'}-\left(\frac{\mathrm{w}}{R}\right)v^2=\frac{Gr_{\mathrm{w}}}{Re_{\mathrm{w}}^2}\sin\theta T^*-\frac{\partial p'}{\partial x'}+\frac{1}{Re_{\mathrm{w}}}\left(\nabla^2 u-\frac{2\mathrm{w}}{R}\frac{\partial v}{\partial y'}\right). \quad (A.4)$$

The Laplacian in this case becomes

$$\nabla^2=\frac{\partial^2}{\partial x'^2}+\frac{\mathrm{w}}{R}\frac{\partial}{\partial x'}+\frac{\partial^2}{\partial y'^2}+\frac{\partial^2}{\partial z'^2}.$$

The same analysis was carried out on the other equations and the results are presented in Table 1 along with the corresponding Boussinesq equations for a rectangular cavity in rectangular coordinates (the dashes have been dropped from the non-dimensional coordinates). From Table 1 it can be seen that the equations for the rectangular and annular cases become almost identical in the limit $\mathrm{w}/R\to 0$. The centripetal force components in the momentum equations disappear, as do some extra derivatives. The only differences are in the buoyancy terms, which are intrinsically different because of the orientation of the geometry relative to gravity. Fig. 15 shows the heat flux as a function of height from numerical simulations, for two different sets of boundary conditions in both an annular mantle heat exchanger and a corresponding rectangular cavity. It can be seen that, even for large values of $Gr_{\mathrm{w}}/Re_{\mathrm{w}}^2$ (700), the heat flux distribution with height for the annular and rectangular geometries is very similar. The major variations are around the bottom and top regions, where the differences in the orientation of the geometries relative to gravity are the greatest. At the bottom around the inlet the annular geometry has the highest heat-transfer rate due to the fact that the inlet impinging jet momentum and buoyancy are in the same direction. The differences in net heat-transfer rate between the annular and rectangular cases shown in Fig. 15 are less than 5%.

References

Bejan, A., 1995. Convection Heat Transfer, second ed.. Wiley, New York.

Dahl, S.D., Davidson, J.H., 1998. Mixed convection heat transfer and pressure drop correlation for tube-in-shell thermosyphon heat exchangers with uniform heat flux. ASME J. Solar Energy Eng. 120, 260–269.

Gao, S., Rahman, M.M., 1999. Analysis of cross-flow mixed convection with applications to building heat transfer. Renewable and Advanced Energy Systems for the 21st Century, Maui, Hawaii, RAE99-7631.

Hattori, N., 1979. Combined free and forced-convection heat-transfer for fully developed laminar flow in horizontal concentric annuli (numerical analysis). Heat Transfer: Jpn. Res. 8 (4), 27–48.

Fluent Inc., 1997. FLUENT 4.4 Users Manual, vol. 1.

Karki, K.C., Patankar, S.V., 1989. Laminar mixed convection in the entrance region of a horizontal annulus. Numer. Heat Transfer 15, 87–99.

Kays, W.M., Crawford, M.E., 1980. Convective Heat and Mass Transfer. McGraw-Hill, New York.

Klein, S.A.. University of Wisconsin, Madison.

Ligrani, P.M., Choi, S., 1996. Mixed convection in straight and curved channels with buoyancy orthogonal to the forced flow. Int. J. Heat Mass Transfer 39 (12), 2473–2484.

Mercer, W.E., Pearce, W.M., Hitchcock, J.E., 1967. Laminar forced convection in the entrance region between parallel flat plates. ASME J. Heat Transfer 89, 251–257.

Morrison, G.L., Nasr, A., Behnia, M., Rosengarten, G., 1998. Analysis of horizontal mantle heat exchangers in solar water heating systems. Solar Energy 64 (1-3), 19–31.

Morrison, G.L., Rosengarten, G., Behnia, M., 1999. Mantle heat exchangers for horizontal tank thermosyphon solar water heaters. Solar Energy 67 (1–3), 53–94.

Neiswanger, L., Johnson, G.A., Carey, V.P., 1987. An experimental study of high Rayleigh number mixed convection in a rectangular enclosure with restricted inlet and outlet openings. ASME J. Heat Transfer 109, 446–453.

Nonio, C., Giudice, S.D., 1996. Finite element analysis of laminar mixed convection in the entrance region of horizontal annular ducts. Numer. Heat Transfer, Part A 29, 313–330.

Rahman, M.M., Carey, V.P., 1990. Experimental measurements of orthogonal mixed convection in a partial enclosure. Int. J. Heat Mass Transfer 33 (6), 1307–1319.

Rosengarten, G., Morrison, G.L., Behnia, M., 1999a. Mixed convection in a narrow rectangular cavity with application to horizontal mantle heat exchangers. Int. J. Energy Res. 23, 1007–1016.

Rosengarten, G., Morrison, G., Behnia, M., 1999b. A second law approach to characterising thermally stratified hot water storage in solar water heaters. ASME J. Solar Energy Eng. 121, 194–200.

Shah, R.K., London, A.L., 1978. Laminar Flow Forced Convection in Ducts. A Source Book for Compact Heat Exchanger Aanalytical Data. Academic Press, New York.

Zenen, S.R., Collins, M.W., Simonson, J.R., 1985. Combined convection in an annulus applied to a thermal storage problem. Int. J. Numer. Methods Eng. 21, 691–711.